Biophysical Review

X-Ray Absorption Spectroscopy of Dinuclear Metallohydrolases

David L. Tierney[1,*] and Gerhard Schenk[2]
[1]Department of Chemistry and Biochemistry, Miami University, Oxford, Ohio; and [2]School of Chemistry and Molecular Biosciences, The University of Queensland, St. Lucia, Queensland, Australia

ABSTRACT In this mini-review, we briefly discuss the physical origin of x-ray absorption spectroscopy (XAS) before illustrating its application using dinuclear metallohydrolases as exemplary systems. The systems we have selected for illustrative purposes present a challenging problem for XAS, one that is ideal to demonstrate the potential of this methodology for structure/function studies of metalloenzymes in general. When the metal ion is redox active, XAS provides a sensitive measure of oxidation-state-dependent differences. When the metal ion is zinc, XAS is the only spectroscopic method that will provide easily accessible structural information in solution. In the case of heterodimetallic sites, XAS has the unique ability to interrogate each metal site independently in the same sample. One of the strongest advantages of XAS is its ability to examine metal ion site structures with crystallographic precision, without the need for a crystal. This is key for studying flexible metal ion sites, such as those described in the selected examples, because it allows one to monitor structural changes that occur during substrate turnover.

INTRODUCTION

Although x-ray absorption was described in the early 1900s (1–5), it was not until the advent of synchrotron light sources in the 1970s that x-ray absorption spectroscopy (XAS) began to realize its potential as a powerful structural tool. Synchrotron sources offer high-intensity light across a wide spectrum (up to ~30 keV or 2×10^8 cm^{-1}, $\lambda =$ 0.4 Å), allowing application of XAS to a wide variety of elements. Synchrotron radiation provides several orders of magnitude more flux density than conventional vacuum tube sources and thus is especially suited to the study of dilute materials, such as metalloproteins in solution (6). XAS offers two key advantages for the study of metalloproteins. The most important of these is its ability to provide details regarding the local structure of a metal ion in frozen solution without the need for crystalline material, which facilitates the study of frozen reaction intermediates. The second advantage is its element specificity, which allows detailed studies of individual metal sites in heterodimetallic systems. Examples highlighting both advantages are discussed further below.

The application of XAS to metalloproteins has grown in frequency and sophistication with subsequent advances in monochromator (7–10) and detector design (11–15), and in the theory used to analyze the data (16–23). The technique itself has been reviewed extensively (6,24–26), along with the strategies associated with data collection (27). In this mini-review, we briefly discuss the physical origin of XAS before illustrating its application using dinuclear metallohydrolases as exemplary systems. The practicalities of data collection and analysis, specific to systems of this type, are addressed in the Supporting Material. The systems we have selected for illustrative purposes present a challenging problem for XAS, one that is ideal to demonstrate the potential of this methodology for structure/function studies of metalloenzymes in general. As the most commonly encountered metal ions in these systems are Zn(II) and Co(II) (as an in vitro replacement for Zn(II) or other biologically relevant metal ions), we will focus our discussion of the technique as applied to these ions.

THEORETICAL BACKGROUND: THE PHYSICAL ORIGIN OF XAS

XAS is a manifestation of the photoelectric effect, where incident light leads to ejection of a core electron, or photoelectron production. The onset of photoelectron production is accompanied by a rapid rise in absorption, referred to as an edge. The type of edge is determined by the principal quantum number associated with the initial state of the photoelectron, as illustrated in Fig. 1, with $n = 1$ (K shell) leading to a K edge and $n = 2$ (L shell) leading to an L edge. The L edge is split because a photoelectron that originates in the $2s$ orbital ($L = 0$, $m_l = 0$; L_1 edge) is different from one that originates in a $2p$ orbital ($L = 1$, $m_l = 0, \pm 1$). The spin-orbit coupling of the $2p^5$ state that is generated from excitation of a $2p$ electron further splits the L edge into L_2 ($m_l = 0$, $m_s = {}^1/_2$, $m_j = {}^1/_2$) and L_3 ($m_l = 1$, $m_s = {}^1/_2$, $m_j = {}^3/_2$) components. Because these are electronic transitions, they are governed by the same selection rules as optical absorption. Consequently, the probability of K-edge absorption is substantially higher than that of L-edge absorption. The degeneracy associated with the L_3 edge makes

Submitted April 22, 2014, and accepted for publication July 24, 2014.

*Correspondence: tiernedl@miamioh.edu

Editor: Brian Salzberg.

0006-3495/14/09/1263/10 $2.00

http://dx.doi.org/10.1016/j.bpj.2014.07.066

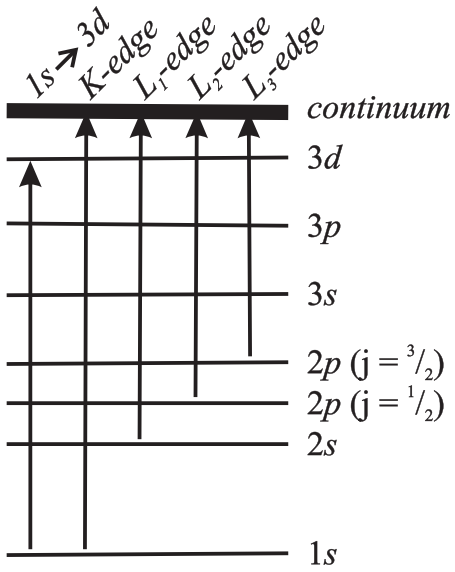

FIGURE 1 Electronic transitions associated with various x-ray edges.

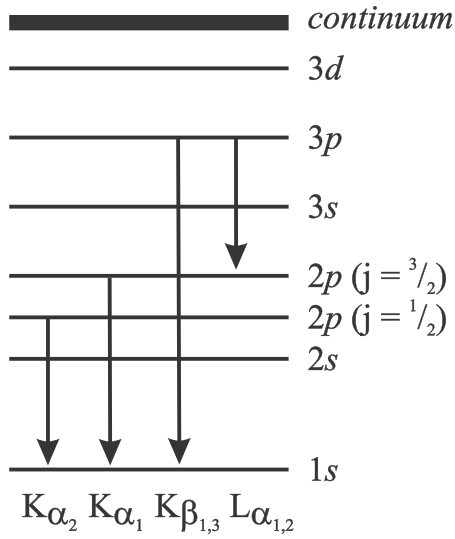

FIGURE 2 Simplified view of common x-ray emission lines.

it twice as probable as L_2. Also indicated in Fig. 1 is the bound state $1s \rightarrow 3d$ transition that is common to open-shell, first-row transition metals (discussed below):

$$I_t = I_0 \exp(-\mu_m \rho t) \quad (1)$$

$$A = \mu t = \ln\left(\frac{I_0}{I_t}\right) \quad (2)$$

At its most basic level, XAS is a simple Beer's law absorption experiment, according to Eq. 1. The transmitted x-ray intensity, I_t, is directly proportional to the incident x-ray intensity, I_0, scaled by the element-specific mass absorption coefficient, μ_m ($cm^2\ g^{-1}$), the density of the sample, ρ ($g\ cm^{-3}$), and the sample thickness, t (cm). The absorbance can be expressed directly as the natural log of the incident intensity divided by the transmitted intensity (Eq. 2). However, the inherently low concentrations encountered in metalloproteins generally render the simple transmission measurement ineffective and one must resort to a more sensitive mode of detection, such as fluorescence.

Emission of a fluorescent photon is the dominant relaxation pathway for high-energy excitation. For lighter atoms of the second period, such as C or O, where the K edge is only a few hundred electronvolts, relaxation more commonly occurs by ejection of an Auger electron. However, for elements of the third period and beyond, where the K edge is greater than a few thousand electronvolts, Auger emission becomes less favorable. A simplified representation of the most common x-ray emission lines is shown in Fig. 2. Because emission occurs at a single, well-defined wavelength, the measurement of fluorescence excitation spectra allows one to use energy-dispersive (discriminating) solid-state detectors, which makes the application of XAS to dilute biomolecules substantially more accessible.

A typical x-ray absorption spectrum, as shown in Fig. 3, can be divided into three distinct regions. Below the threshold (edge) energy of a given element (E_0), the incident x-ray photon has insufficient energy to cause core-electron ejection, and only background absorption from lighter elements in the sample matrix is observed. Historically, the region within approximately ± 25 eV of the absorption edge ($E \sim E_0$) is referred to as the x-ray absorption near-edge structure (XANES; the energy limits are somewhat arbitrary). This area of the spectrum is often called the near-edge x-ray absorption fine structure (NEXAFS) in the materials science literature, especially when dealing with lighter atoms. The extended x-ray absorption fine structure (EXAFS; $E > E_0$) region begins 20–50 eV beyond the absorption edge, continuing to higher energy. The acronym XAFS (for x-ray absorption fine structure) is often used in the literature as an umbrella term encompassing the fine structure associated with both the XANES and the EXAFS. The information content of the XANES and EXAFS is discussed in more detail in the following sections, and the

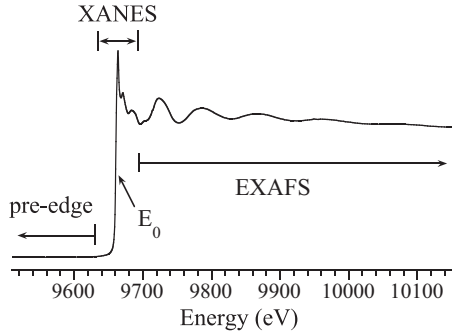

FIGURE 3 Example of an as-collected x-ray absorption spectrum at the Zn K edge.

methods necessary to extract this information are discussed in the Supporting Material.

XANES

The structure superimposed on the rising edge, observed in the XANES region of the spectrum, is due to transitions to unfilled molecular orbitals and continuum resonances, where the unbound final state is strongly perturbed by the electronic potentials of both the absorber and the surrounding atoms. Consequently, the shape and relative intensity of the XANES are indicative of the electronic structure and coordination geometry of the absorbing atom. Although investigators have made significant strides in developing the theory that describes the XANES (28–31), in practice, most still utilize this part of the spectrum as a fingerprint. The energy of the absorption edge effectively represents the metal ion's ionization potential in the complex. Therefore, it is highly dependent on the oxidation state, typically shifting by ~2 eV to higher energy per electron removed (24,32–35), and, to a lesser degree, on the composition of the donor set. The subtle differences in shape that accompany a change in environment are often more easily visualized by examining the derivative of the XANES (35).

For open-shell systems (d^0–d^9), bound-state transitions are often observed just below E_0. The $1s \rightarrow 3d$ transition that is typical of open-shell, first-row transition metals is forbidden by dipole selection rules. However, this transition is quadrupole allowed and therefore always exhibits some finite intensity. The $1s \rightarrow 3d$ transition becomes increasingly dipole allowed with increasing departure from centrosymmetry, due to greater mixing of the metal $3d$ and $4p$ orbitals. A quantitative comparison of XANES spectra requires prior normalization, which is usually accomplished by fitting a polynomial and scale factor to the data below and well above the edge (36), and scaling the result to match the atomic mass absorption coefficient (see Supporting Material for details) (37). The result of this procedure is an x-ray absorption spectrum whose edge jump is equivalent to that expected for a single atom in that environment.

Isolation of the $1s \rightarrow 3d$ transition from the rising absorption edge is typically accomplished by fitting a quadratic polynomial to the region immediately below the transition and an arctangent to the rising edge, above the transition, as illustrated in Fig. 4. The $1s \rightarrow 3d$ area is then calculated by numerical integration and divided by the mass absorption coefficient. In the case of Fe(II) and Fe(III) complexes, the intensity of the $1s \rightarrow 3d$ transition has been shown to be highly correlated with the metal coordination number, with the lowest intensity for six-coordinate Fe and the highest intensity for four-coordinate Fe (32,33). Similar correlations have been defined for Mn (38), Ni (39–41), and Co (see Fig. 4). The edge structure for Cu-containing systems is also diagnostic, but on a more complicated level. In contrast, as a closed-shell $3d^{10}$ ion, Zn(II) shows no pre-

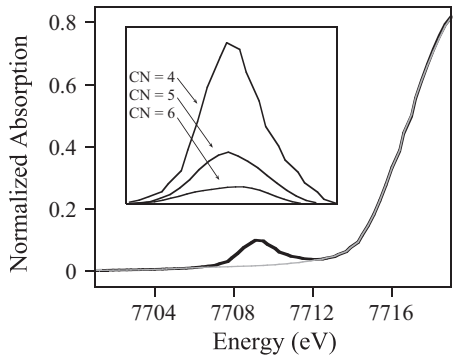

FIGURE 4 Co(II) XANES fit. Inset: trend in 1s → 3d intensity for four-, five-, and six-coordinate Co(II).

edge transitions, and only a slight dependence on coordination geometry and the composition of the donor set. In general, the first oscillation above the edge decreases in intensity relative to the white line, as the amount of sulfur donation increases (Fig. 5), and the white line increases with increasing coordination number.

EXAFS

In contrast to XANES, the theory describing EXAFS is well established (16–23). As the energy of the incident x-ray photon increases, above E_0, the excess photon energy is converted to kinetic energy of the photoelectron. In K-edge spectroscopy, where the initial state is the absorbing atom's $1s$ orbital, the ejected electron has an equal probability of propagating in any direction, allowing the photoelectron to be treated as a spherical wave with a characteristic de Broglie wavelength, $\lambda = h/m_e v = 2hc/m_e v^2$.

As the photoelectron radiates from the absorbing atom, there is a finite probability that it will encounter nearby atoms, scattering off of the nuclei. It is this scattering event that leads to modulation of the x-ray absorption coefficient, which arises from the interaction of the outgoing and backscattered photoelectron waves. The absorption coefficient is modulated by the amplitude of the backscattered

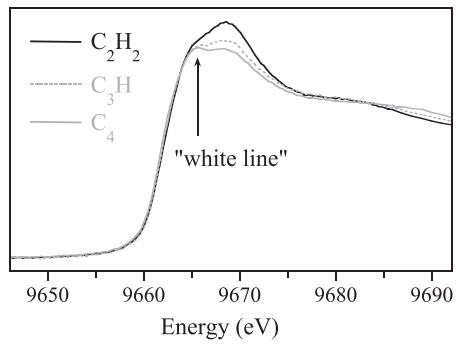

FIGURE 5 Four-coordinate Zn XANES spectra, with cys_2his_2, cys_3his, and cys_4 donor sets.

photoelectron wave at the absorbing atom. As the incident x-ray energy is increased and the wavelength of the photoelectron is decreased, the outgoing and backscattered waves pass through regions of constructive and destructive interference. This results in local maxima and minima, respectively, in the absorption cross section (Fig. 6). When the photoelectron wavelength reaches an integer multiple of the absorber-scatterer interatomic distance, the outgoing and backscattered waves reinforce each other, enhancing the absorption cross section and resulting in a local maximum. As the two waves lose phase identity, they effectively cancel each other and a minimum in absorption is observed.

The strength of the EXAFS lies in the precision and accuracy of the structural parameters that can be extracted from the data. This process (described in detail in the Supporting Material) entails background subtraction steps to first remove absorption by lighter elements and then the smoothly decaying atomic absorption of the atom of interest to isolate the oscillatory portion of the spectrum (the EXAFS), which contains the local structural information. The EXAFS amplitude is indicative of coordination number and scatterer size, whereas the frequencies report on absorber-scatterer distances, and a structural model is developed and tested by detailed curve fitting. The inherent distance resolution in any data set is limited by the energy range of the data ($\Delta R \sim \pi/2\Delta k$). Historically, the low signal/noise ratio at high k has limited EXAFS studies of metalloproteins to $\Delta k \leq 15$ Å^{-1}, or ΔR ~0.1 Å. Within this limit, it is extremely difficult to extract angular information for all but the simplest systems.

In practice, the accuracy of an EXAFS-derived average first shell bond length is ± 0.02 Å for a group of similar scatterers, and this average first shell bond length has been shown to be a reliable indicator of coordination number (42) (better than the variable in curve fitting, which has an uncertainty of ± 1). As shown in the Supporting Material, low-Z scatterers (nitrogen and oxygen) are difficult to distinguish from each other due to their similarity in size, but they are easily distinguished from larger atoms, such as sulfur. For the dinuclear examples discussed below, the analysis is complicated by the presence of multiple metal-binding sites (as a bulk technique, the EXAFS will measure the average coordination sphere), and for many studies, which hinge on detection of the metal-metal separation, it is further complicated by a background of multiple-scattering interactions from multiple coordinated histidines. A strategy for dealing with this complexity is outlined in the Supporting Material.

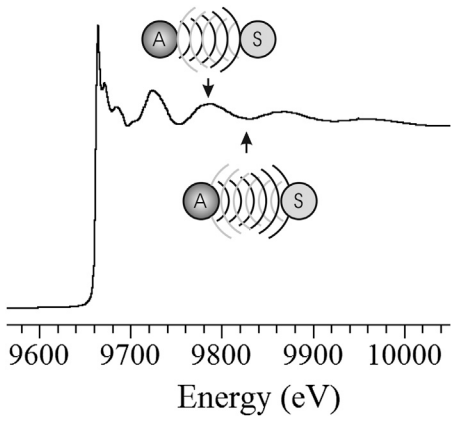

FIGURE 6 Phases associated with local maxima (top) and minima (bottom) in an x-ray absorption spectrum. Atom A represents the absorber, and atom S represents the scatterer.

APPLICATION TO DINUCLEAR METALLOHYDROLASES

Dinuclear hydrolases encompass a vast array of enzymes with widely varying chemistry. Rather than attempt to review all cases that have been examined by XAS, we will restrict the following discussion to just a few in which XAS has made the most significant contributions. XAS has been used to study several aminopeptidases (N-terminal protein degradation) (43,44), AMP deaminase (nucleic acid metabolism) (45–47), prolidase (iminopeptidase) (48), DapE (bacterial peptidoglycan synthesis) (49), arginase (part of the urea cycle) (38,50), the acyl-homoserinelactone (AHL) lactonase (bacterial quorum sensing) (51,52), ZiPD (an RNA processing enzyme with phosphodiesterase activity) (53–56), and glyoxalase (detoxification of α-ketoaldehydes) (57,58). However, for the sake of brevity, we will focus our review on the use of XAS to study purple acid phosphatases (PAPs) and metallo-β-lactamases (MβLs).

PAPs

Phosphatases in general catalyze the hydrolysis of phosphate esters. There are a number of variations within this theme. For example, alkaline phosphatase is a nonspecific monoesterase, and its active-site structure has been examined by XAS (59). The dinuclear metal ion cluster in alkaline phosphatase is unusual in that it is not a cluster in the resting state (i.e., there is no bridge connecting the two catalytic Zn(II) ions). Only one of the two metal ions is required for enzymatic activity, and the other one dramatically enhances the turnover rate. Upon turnover, the product (inorganic phosphate) bridges the two metal ions. Mangani et al. (59) used EXAFS data to examine the effect of the population of the cocatalytic B site on the structure at the catalytic A site. Their study was one of the earliest to take direct advantage of the element specificity of XAS, along with the different binding affinities of the two catalytic sites. By comparing enzyme containing one equivalent of Zn(II) in the tighter-binding catalytic site (all Zn_A) with enzyme that had been preloaded with Zn(II) and supplemented with Co(II) (Zn_ACo_B), they obtained Zn K-edge EXAFS

data that reported only on the local structure of Zn(II) in the A site. The data showed that the presence or absence of metal in the B site had no effect on the local structure of the A site.

By comparison, a considerably greater amount of mechanistic detail has been gleaned from EXAFS studies on PAPs, enzymes that hydrolyze a broad range of phosphorylated substrates (60,61). These enzymes are ubiquitous, having been isolated originally from bovine spleen (BSPAP), kidney bean (KBPAP), and porcine uterus (uteroferrin (Uf)). They have since been isolated from a number of other plant and animal species, including humans, where they have been suggested to play a role in iron transport, macrophage activation, and bone resorption. The active site common to all PAPs is a multiply bridged dinuclear center, which incorporates a pair of iron atoms in mammalian PAPs and a heterodinuclear Fe(III)-M(II) (M = Zn or Mn) cluster in plants.

XAS of bovine PAP was used very early on to determine that both metal ions were six-coordinate in a multiply bridged cluster (62), well in advance of the first crystal structure of any PAP (63). These initial studies further identified a directly coordinated phosphate, which was later shown to be bridging by crystallography (64), as illustrated in Fig. 7. The oxidation-state change, from Fe(II)/Fe(III) (*pink*) to Fe(III)/Fe(III) (*purple*), was confirmed by a 2 eV shift in the edge inflection, and the $1s \rightarrow 3d$ peak areas were used to confirm six coordination for both metal ions.

EXAFS studies of the phosphate and arsenate complexes of the oxidized, diferric form of Uf provided strong evidence of the lack of a μ-oxo bridge, based on the lack of a short Fe-O distance, making Uf distinct from similar systems such as methane monooxygenase (65). The Fe-Fe distances observed (3.22 Å in the phosphate complex and 3.29 Å in the arsenate complex), together with Fe-P and Fe-As distances and associated angular constraints, were interpreted as arising from a bidentate bridging oxyanion. In the reduced form of the enzyme, the Fe-Fe distance increased to ~3.5 Å, which was suggested to be indicative of a carboxylate shift, such that a bridging bidentate carboxylate in the reduced enzyme becomes a monodentate, nonbridging ligand in the oxidized enzyme to make room for the bridging oxyanion. These studies highlight one of the most important advantages offered by XAS, which is the ability to carefully monitor the oxidation state in redox active enzymes. As noted above, the edge position is indicative of the oxidation state, providing a sensitive internal reference.

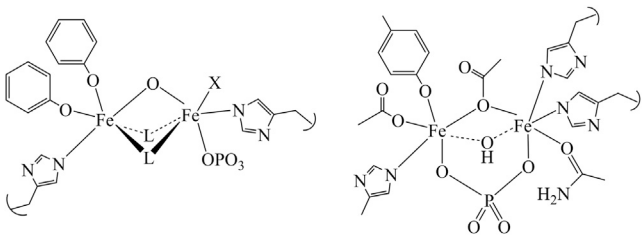

FIGURE 7 PAP active-site structure derived from XAS (left) and x-ray diffraction (1UTE, right).

Although similar studies of native Fe/Zn PAPs, such as those found in plants, have not yet been reported, several studies of a metal-substituted form of porcine PAP (Uf) have been performed. In one study, resting Fe(III)Zn(II) enzyme showed six-coordinate Fe and Zn sites with a metal-metal separation of ~3.3 Å (66). Addition of phosphate left the primary coordination spheres and the metal-metal separation unchanged, with the appearance of a new outer-shell feature that could be attributed to metal-phosphorous scattering. The similarity of the M-P distances clearly showed that the phosphate bridges the two metals in a bidentate fashion (66). A later study showed that molybdate (MoO_4^-) and tungstate (WO_4^-), which inhibit the enzyme, formed similar bridging structures but with asymmetric cores, based on Zn-Mo(W) distances that were ~0.4 Å longer than the associated Fe-Mo(W) distances (67). Together with electron paramagnetic resonance (EPR) and resonance Raman spectroscopy, XAS of the ternary complex of FeZnUf with phosphate and fluoride showed that F^- replaced a hydroxo bridge, based on contraction of the Fe and expansion of the Zn metal-ligand bond lengths (68). Based on these results, Wang et al. (68) suggested that the bridging hydroxide that is replaced by fluoride serves as the nucleophile in substrate turnover. More recent studies of the Fe(III)Ni(II) form of the enzyme supported this proposal (69). These four studies highlight the element specificity of XAS and its unique ability to examine both sites in a heterodimetallic center independently of each other, effectively doubling the available structural and mechanistic detail.

MβLs

The MβLs are a group of enzymes that confer bacterial resistance to penicillins and related β-lactam-containing antibiotics. These ubiquitous enzymes require one or two Zn(II) ions for catalytic activity and are generally unaffected by clinical inhibitors of the related serine β-lactamases (70,71). Approximately 50 MβLs have been reported, leading to their further classification into three subgroups (Fig. 8) (72,73). The B1 MβLs require two Zn(II) ions for full activity and prefer penicillins as substrates. They bind one Zn(II) in what is referred to as the Zn_1 (or 3H) site, which is made up of three histidine side chains and a solvent-derived ligand that bridges the two metal ions. The second Zn(II)-binding site, referred to as the Zn_2 (or DCH) site, consists of one histidine, one cysteine, a monodentate carboxylate, the bridging solvent, and a terminally bound water. The B2 enzymes require only one Zn(II) for full activity (they are actually inhibited by a second

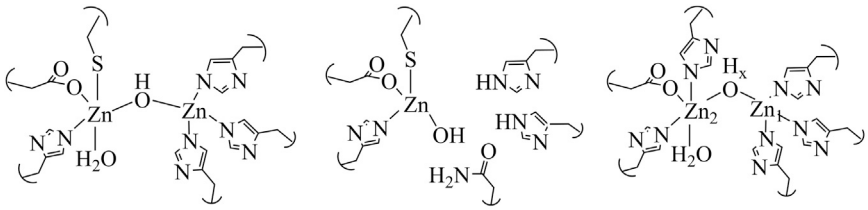

FIGURE 8 General structures for the three subclasses of MβLs.

equivalent of Zn(II)), bind the catalytic Zn(II) in the Zn_2 site, and prefer carbapenems as substrates. The B3 enzymes, which prefer cephalosporins as substrates, generally require two Zn(II) ions for full activity, binding one Zn(II) in a canonical Zn_1 site and one Zn(II) in a modified Zn_2 site, where the cysteine is replaced by another histidine. Much of the mechanistic detail that has been derived for the MβLs has come from parallel studies of the native Zn(II) and Co(II)-substituted enzymes.

Although there remains some debate regarding the physiologically relevant level of metal loading, it is widely accepted that all three subclasses are active with one equivalent of bound Zn(II), with the second equivalent improving the catalytic efficiency of the B1 and B3 enzymes. In light of these observations, the distribution of metal ions as the site is loaded and the individual role each plays in catalysis become critical issues for understanding the mechanism of antibiotic hydrolysis. The earliest application of XAS to the class B1 MβL from *Bacillus cereus* (BcII) identified the presence of sulfur in the zinc coordination sphere, but did not correlate this with metal loading (74). A later study of BcII containing 1.2 equivalents of Zn(II) showed fractional sulfur coordination (0.5 S per Zn), which was interpreted as partial occupancy of the Zn_2 site together with a small population of dinuclear enzyme (75). A subsequent study examined BcII containing one or two equivalents of Zn(II) and found that the first equivalent of metal was evenly distributed between the two metal-binding sites (76). XAS has also played a central role in a number of mutational analyses of BcII that were designed to delineate the factors that separate the MβL subclasses (77–79), but these studies are beyond the scope of this review.

It has since been shown that the minor differences in the two microscopic binding constants for BcII lead to near-statistical scrambling of the metal ions, with the presence of fully loaded, dinuclear enzyme being detected at substoichiometric metal concentrations (80,81), as predicted by the earlier EXAFS studies. A recent EXAFS titration of both Zn(II)- and Co(II)-loaded BcII generalized these results and clearly showed the presence of dinuclear enzyme with as little as 0.5 equivalents of metal per protein regardless of the metal ion (82). Similar behavior was seen in the B1 MβL IMP-1, which clearly showed distributed metal binding with one equivalent of added Zn(II) (83). The lack of significant metal-metal scattering suggests that this is not reflective of cooperativity. In contrast, Co(II) binding does appear to be cooperative, with dinuclear enzyme (indicated by significant metal-metal scattering) observed with one equivalent of added Co(II). Aside from minor differences, the binding sites in native (Zn(II)-bound) and Co(II)-substituted BcII and IMP-1 appear to be the same. XAS was similarly used to establish the distributed binding of Co(II) by the B1 MβL NDM-1 (84).

Unlike BcII and IMP-1, the B1 enzyme CcrA from *Bacillus fragilis* binds both Zn(II) and Co(II) sequentially, first fully loading the Zn_1 (3H) site and then populating the Zn_2 site. This has been shown through a combination of EXAFS, UV-Vis, EPR, and NMR spectroscopies (85,86). Similar behavior has been observed for the B3 enzyme L1 from *Stenotrophomonas maltophilia* (87). In each of these cases, it was shown that the Co(II)-bound form is slightly different from the native Zn(II) enzymes. The Co K-edge EXAFS for each enzyme indicated an expanded coordination sphere relative to the corresponding Zn(II) enzymes, most likely reflecting the incorporation of an extra solvent ligand by each metal ion in the Co(II)-containing enzymes. The lack of metal-metal scattering suggested that the di-Co(II) enzymes were not bridged, as is commonly observed in studies of MβLs. Interestingly, the absence of a bridge does not appear to affect the catalytic ability of the enzymes.

Distinct from all of the above examples is the B1 MβL from *Bacillus anthracis* (Bla2), which showed different metal-binding behaviors depending on whether the metal added was Zn(II) or Co(II) (86). Whereas Bla2 was shown to bind Zn(II) sequentially, similar to what was found for CcrA and L1, it clearly bound Co(II) in an indiscriminate manner, loading each site equally regardless of stoichiometry, thus resembling BcII, IMP-1, and NDM-1. Although it shares 89% sequence identity with BcII, the *B. anthracis* MβL provides a unique example of how small changes in outer-sphere residues can alter the metal-binding properties of an enzyme and tune its selectivity. The above results are summarized in Table 1.

EXAFS data recorded for the B2 MβL imiS from *A. veronii* shed light on the mechanism of metal ion inhibition, whose origin had not been previously understood (88). In the presence of one equivalent of Zn(II), the EXAFS of imiS was clearly consistent with the metal site defined by crystallography, with the metal ion bound at the Zn_2 site, including one cysteine sulfur and one histidine. When the

TABLE 1 Metal-binding behavior of dinuclear MβLs defined by XAS

Enzyme	Zn(II) binding	Co(II) binding	Co(II) coordination expansion	Zn-Zn separation	Co-Co separation	References
BcII (B1)	Scrambled scrambled	Scrambled	no	3.42 Å 3.70 Å	3.55 Å	(74,75,81)
IMP-1 (B1)	scrambled	scrambled	no	3.39 Å	3.45 Å	(82)
NDM-1 (B1)		scrambled	no	3.38 Å	3.45 Å (ZnCo) 3.51 Å (CoCo) 3.56 Å (CoCd)	(83,90)
CcrA (B1)	sequential	sequential	yes	3.44 Å	not detected	(84,85)
Bla2 (B1)	sequential	scrambled	yes	3.44 Å	not detected	(85)
L1 (B3)	sequential	sequential	yes	3.42 Å	not detected	(86)

enzyme in the presence of two equivalents of Zn(II) was examined, it was found that the level of sulfur contribution to the Zn K-edge EXAFS was the same (1.0 S/Zn), suggesting that the inhibitory site also included a sulfur ligand. A scan of the primary sequence of imiS revealed that the active-site cysteine was the only cysteine in the protein. However, several methionine residues were identified, including one that resides in the middle of an α-helix that was later shown to be mobile during substrate turnover (89), directly across from a histidine on the surface of the protein. Mutation of this methionine to an isoleucine fully abolished metal ion inhibition in imiS. A survey of MβL primary sequences showed that this methionine is only present in the B2 subclass, with no analog in the unstructured loops of B1 and B3 enzymes.

Two recent applications (90) frame the two areas where XAS can provide particularly unique information. The first focused on the reaction of L1 with substrate, opening a new line of research in this area. Earlier EXAFS studies of L1 included its product complex with hydrolyzed nitrocefin and showed that after hydrolysis, the bound product rotated in the active-site pocket, forming an unanticipated Zn-S bond (Fig. 9) (87). The Zn-Zn separation increased by 0.2 Å (from 3.42 Å to 3.62 Å) upon formation of this product complex. A later EXAFS examination of L1, freeze-quenched after 10 ms of reaction with nitrocefin, showed an even longer metal-metal separation of 3.72 Å (90). Together, these observations show that the transfer of physical stresses imparted by protein-associated motions may aid in the ring-opening reaction catalyzed by dinuclear MβLs.

The second recent development involves the preparation of a series of homogeneous heterodimetallic forms of the B1 MβL NDM-1 (84). It was shown that by incubating the apoenzyme with one equivalent of either Zn(II) or Cd(II), followed by addition of one equivalent of Co(II), one can prepare heterodimetallic forms with fidelity, taking advantage of the similarity of the Zn_1 and Zn_2 sites' affinities for Co(II) and their drastically different affinities for Zn(II), which loads the Zn_1 site, and Cd(II), which loads the Zn_2 site. This represents an important extension of the above studies because it affords the opportunity to exploit the element specificity of XAS, as described above for the mixed-metal phosphatases. A comparison of the four forms of NDM-1 (ZnZn, ZnCo, CoCo, and CoCd) showed nearly identical kinetic constants (within a factor of 5), and the metal-metal separations were shown to track nicely with the covalent radii of the metals involved, ranging from 3.38 to 3.56 Å (84,91) (see Table 1). Together, these two developments may enable investigators to study time-dependent local structure by specifically interrogating each side of an MβL dinuclear cluster independently in the same sample.

CONCLUSIONS

The above examples are not meant to comprise an exhaustive review, but rather to illustrate how XAS can contribute to the study of dinuclear hydrolytic enzymes. When the metal ion is redox active, XAS provides a sensitive measure of oxidation-state-dependent differences. When the metal ion is zinc, XAS is the only spectroscopic method that will provide easily accessible structural information in solution. In the case of heterodimetallic sites, XAS has the unique ability to interrogate each metal site independently in the same sample. One of the strongest advantages of XAS is its ability to examine metal site structure with crystallographic precision, without the need for a crystal. This is key for studying flexible metal sites such as those described above because it allows one to monitor structural

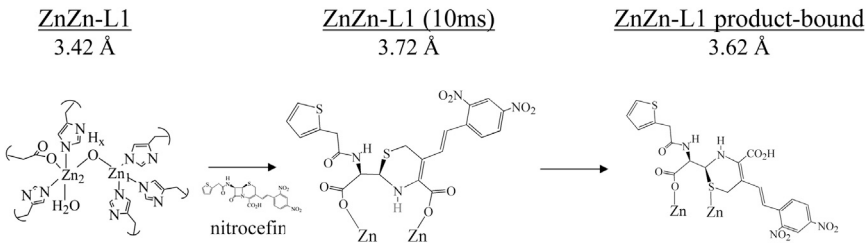

FIGURE 9 Variations in the structure of L1 during hydrolysis of nitrocefin, determined by EXAFS.

changes that occur during substrate turnover. The metrical parameters provided by XAS are a critical link between solution and crystallographic structure, and allow for deeper interrogation of these systems using other techniques, as demonstrated above for Uf. For Zn(II)-containing systems, XAS may serve as the only available source of structural information in the absence of diffraction-quality crystals.

SUPPORTING MATERIAL

Nine figures, and supplemental information are available at http://www.biophysj.org/biophysj/supplemental/S0006-3495(14)00815-7.

G.S. received a Future Fellowship (FT120100694) from the Australian Research Council.

SUPPORTING CITATIONS

References (92–104) appear in the Supporting Material.

REFERENCES

1. Bragg, W. H. 1914. An X-ray absorption band. *Nature.* 93:31–32.
2. deBroglie, M., and A. Dauvillier. 1920. The fine structure of the discontinuities in X-ray absorption spectra. *Compt. Rend.* 171:626–627.
3. Lindh, A. E. 1921. The X-ray absorption spectra of chlorine. *Compt. Rend.* 172:1175–1176.
4. Richtmyer, F. K. 1921. Mass-absorption coefficients as a function of wave length above and below the K X-ray limit of the absorber. *Phys. Rev.* 17:264–265.
5. Siegbahn, M. 1925. The Spectroscopy of X-Rays. Oxford University Press, New York.
6. Scott, R. A. 1985. Measurement of metal-ligand distances by EXAFS. *Methods Enzymol.* 117:414–459.
7. Depautex, C., P. Thiry, …, J. Flamand. 1978. A new design for high flux grazing incidence monochromator for synchrotron radiation. *Nucl. Instrum. Methods.* 152:101–102.
8. Deslattes, R. D. 1980. X-ray monochromator development for synchrotron radiation facilities. *Nucl. Instrum. Methods.* 172:201–208.
9. Sparks, Jr., C. J., B. S. Borie, and J. B. Hastings. 1980. X-ray monochromator geometry for focusing synchrotron radiation above 10 keV. *Nucl. Instrum. Methods.* 172:237–242.
10. Golovchenko, J. A., R. A. Levesque, and P. L. Cowan. 1981. X-ray monochromator system for use with synchrotron radiation sources. *Rev. Sci. Instrum.* 52:509–516.
11. Lytle, F. W., R. B. Greegor, …, F. E. Huggins. 1984. Measurement of soft x-ray absorption spectra with a fluorescent ion chamber detector. *Nucl. Instrum. Methods Phys. Res. A.* 226:542–548.
12. Cramer, S. P., and R. A. Scott. 1981. New fluorescence detection system for x-ray absorption spectroscopy. *Rev. Sci. Instrum.* 52:395–399.
13. Cramer, S. P., O. Tench, …, G. N. George. 1988. A 13-element germanium detector for fluorescence EXAFS. *Nucl. Instrum. Methods Phys. Res. A.* A266:586–591.
14. Furenlid, L. R., H. W. Kraner, …, J. Beren. 1992. The NSLS 100 element solid state array detector. *Nucl. Instrum. Methods Phys. Res. A.* A319:408–413.
15. Suzuki, M., N. Kawamura, …, T. Ishikawa. 2002. Fast multigrid fluorescent ion chamber with 0.1 ms time response. *J. Synchrotron Radiat.* 9:99–102.
16. Sayers, D. E., E. A. Stern, and F. W. Lytle. 1971. New technique for investigating noncrystalline structures: Fourier analysis of the extended x-ray-absorption fine structure. *Phys. Rev. Lett.* 27:1204–1207.
17. Stern, E. A., D. E. Sayers, and F. W. Lytle. 1975. Extended x-ray-absorption fine-structure technique. III. Determination of physical parameters. *Phys. Rev. B.* 11:4836–4846.
18. Stern, E. A. 1988. X-ray absorption: principles, applications, techniques of EXAFS, SEXAFS and XANES. *In* Chemical Analysis, *Vol. 92*. D. C. Koningsberger, and R. Prins, editors. John Wiley & Sons, New York.
19. Rehr, J. J., R. C. Albers, …, E. A. Stern. 1986. New high-energy approximation for x-ray-absorption near-edge structure. *Phys. Rev. B Condens. Matter.* 34:4350–4353.
20. Gurman, S. J. 1989. Spherical wave theories of EXAFS. *Physica B.* 158:359–361.
21. Vaarkamp, M., I. Dring, …, D. C. Koningsberger. 1994. Comparison of theoretical methods for the calculation of extended x-ray-absorption fine structure. *Phys. Rev. B Condens. Matter.* 50:7872–7883.
22. Binsted, N., and S. S. Hasnain. 1996. State-of-the-art analysis of whole x-ray absorption spectra. *J. Synchrotron Radiat.* 3:185–196.
23. Rehr, J. J., J. J. Kas, …, K. Jorissen. 2010. Parameter-free calculations of X-ray spectra with FEFF9. *Phys. Chem. Chem. Phys.* 12:5503–5513.
24. Riggs-Gelasco, P. J., T. L. Stemmler, and J. E. Penner-Hahn. 1995. XAFS of dinuclear metal sites in proteins and model compounds. *Coord. Chem. Rev.* 144:245–286.
25. Penner-Hahn, J. E. 1999. X-ray absorption spectroscopy in coordination chemistry. *Coord. Chem. Rev.* 190–192:1101–1123.
26. Penner-Hahn, J. E. 2005. Characterization of "spectroscopically quiet" metals in biology. *Coord. Chem. Rev.* 249:161–177.
27. Ascone, I., W. Meyer-Klaucke, and L. Murphy. 2003. Experimental aspects of biological X-ray absorption spectroscopy. *J. Synchrotron Radiat.* 10:16–22.
28. Rehr, J. J., and A. L. Ankudinov. 2005. Progress in the theory and interpretation of XANES. *Coord. Chem. Rev.* 249:131–140.
29. Benfatto, M., J. A. Solera, …, J. Garcia. 1997. Theoretical analysis of x-ray absorption near-edge structure of transition-metal aqueous complexes in solution at the metal K edge. *Phys. Rev. B.* 56:2447–2452.
30. Modrow, H., S. Bucher, J. J. Rehr, and A. L. Ankudinov. 2003. Calculation and interpretation of K-shell X-ray absorption near-edge structure of transition metal oxides. *Phys. Rev. B.* 67:035123.
31. D'Angelo, P., A. Lapi, …, S. Della-Longa. 2008. X-ray absorption spectroscopy of hemes and hemeproteins in solution: multiple scattering analysis. *Inorg. Chem.* 47:9905–9918.
32. Randall, C. R., L. Shu, …, L. Que, Jr. 1995. X-ray absorption studies of high-spin iron(II) complexes. *Inorg. Chem.* 34:1036–1039.
33. Roe, A. L., D. J. Schneider, …, L. Que, Jr. 1984. X-ray absorption spectroscopy of iron-tyrosinate proteins. *J. Am. Chem. Soc.* 106:1676–1681.
34. Srivastava, U. C., and H. L. Nigam. 1972. X-ray absorption edge spectrometry as applied to coordination chemistry. *Coord. Chem. Rev.* 9:275–310.
35. Tierney, D. L., J. A. Fee, …, J. E. Penner-Hahn. 1995. X-ray absorption spectroscopy of the iron site in *Escherichia coli* Fe(III) superoxide dismutase. *Biochemistry.* 34:1661–1668.
36. Waldo, G. S., R. M. Fronko, and J. E. Penner-Hahn. 1991. Inactivation and reactivation of manganese catalase: oxidation-state assignments using X-ray absorption spectroscopy. *Biochemistry.* 30:10486–10490.
37. McMaster, W. H., N. Kerr del Grande, …, J. H. Hubbell. 1969. Compilation of X-Ray Cross Sections. Lawrence Radiation Laboratory, Livermore, CA.
38. Stemmler, T. L., T. M. Sossong, Jr., …, J. E. Penner-Hahn. 1997. EXAFS comparison of the dimanganese core structures of manganese catalase, arginase, and manganese-substituted ribonucleotide reductase and hemerythrin. *Biochemistry.* 36:9847–9858.

39. Eidsness, M. K., R. J. Sullivan, …, R. A. Scott. 1986. Structure diversity of F430 from *Methanobacterium thermoautotrophicum*. A nickel x-ray absorption spectroscopic study. *J. Am. Chem. Soc.* 108:3120–3121.

40. Baidya, N., M. M. Olmstead, …, P. K. Mascharak. 1992. X-ray absorption spectra of nickel complexes with N_3S_2 chromophores and spectroscopic studies on hydride and carbon monoxide binding at these nickel centers: relevance to the reactivity of the nickel site(s) in [FeNi] hydrogenases. *Inorg. Chem.* 31:3612–3619.

41. Shearer, J., A. Dehestani, and F. Abanda. 2008. Probing variable amine/amide ligation in Ni(II)N_2S_2 complexes using sulfur K-edge and nickel L-edge X-ray absorption spectroscopies: implications for the active site of nickel superoxide dismutase. *Inorg. Chem.* 47:2649–2660.

42. Thorp, H. H. 1992. Bond valence sum analysis of metal-ligand bond lengths in metalloenzymes and model complexes. *Inorg. Chem.* 31:1585–1588.

43. Zhang, L., M. J. Crossley, …, H. C. Freeman. 1998. Spectroscopic identification of a dinuclear metal centre in manganese(II)-activated aminopeptidase P from *Escherichia coli*: implications for human prolidase. *J. Biol. Inorg. Chem.* 3:470–483.

44. Cosper, N. J., V. M. D'souza, …, R. C. Holz. 2001. Structural evidence that the methionyl aminopeptidase from *Escherichia coli* is a mononuclear metalloprotease. *Biochemistry.* 40:13302–13309.

45. Mangani, S., W. Meyer-Klaucke, …, A. Raggi. 2003. Characterization of the zinc-binding site of the histidine-proline-rich glycoprotein associated with rabbit skeletal muscle AMP deaminase. *J. Biol. Chem.* 278:3176–3184.

46. Mangani, S., M. Benvenuti, …, A. Raggi. 2007. Characterization of the metallocenter of rabbit skeletal muscle AMP deaminase. Evidence for a dinuclear zinc site. *Biochim. Biophys. Acta.* 1774:312–322.

47. Martini, D., M. Ranieri-Raggi, …, A. Raggi. 2007. Characterization of the metallocenter of rabbit skeletal muscle AMP deaminase. A new model for substrate interactions at a dinuclear cocatalytic Zn site. *Biochim. Biophys. Acta.* 1774:1508–1518.

48. Besio, R., S. Alleva, …, S. Morante. 2010. Identifying the structure of the active sites of human recombinant prolidase. *Eur. Biophys. J.* 39:935–945.

49. Cosper, N. J., D. L. Bienvenue, …, R. C. Holz. 2003. The dapE-encoded N-succinyl-l,l-diaminopimelic acid desuccinylase from *Haemophilus influenzae* is a dinuclear metallohydrolase. *J. Am. Chem. Soc.* 125:14654–14655.

50. Stone, E. M., E. S. Glazer, …, G. Georgiou. 2010. Replacing Mn(2+) with Co(2+) in human arginase I enhances cytotoxicity toward l-arginine auxotrophic cancer cell lines. *ACS Chem. Biol.* 5:333–342.

51. Momb, J., P. W. Thomas, …, W. Fast. 2006. The quorum-quenching metallo-γ-lactonase from *Bacillus thuringiensis* exhibits a leaving group thio effect. *Biochemistry.* 45:13385–13393.

52. Thomas, P. W., E. M. Stone, …, W. Fast. 2005. The quorum-quenching lactonase from *Bacillus thuringiensis* is a metalloprotein. *Biochemistry.* 44:7559–7569.

53. Vogel, A., O. Schilling, …, W. Meyer-Klaucke. 2002. *ElaC* encodes a novel binuclear zinc phosphodiesterase. *J. Biol. Chem.* 277:29078–29085.

54. Vogel, A., O. Schilling, and W. Meyer-Klaucke. 2004. Identification of metal binding residues for the binuclear zinc phosphodiesterase reveals identical coordination as glyoxalase II. *Biochemistry.* 43:10379–10386.

55. Schilling, O., A. Vogel, …, W. Meyer-Klaucke. 2005. Zinc- and iron-dependent cytosolic metallo-β-lactamase domain proteins exhibit similar zinc-binding affinities, independent of an atypical glutamate at the metal-binding site. *Biochem. J.* 385:145–153.

56. Späth, B., F. Settele, …, A. Marchfelder. 2007. Metal requirements and phosphodiesterase activity of tRNase Z enzymes. *Biochemistry.* 46:14742–14750.

57. Schilling, O., N. Wenzel, …, W. Meyer-Klaucke. 2003. Flexible metal binding of the metallo-β-lactamase domain: glyoxalase II incorporates iron, manganese, and zinc *in vivo*. *Biochemistry.* 42:11777–11786.

58. Wenzel, N. F., A. L. Carenbauer, …, M. W. Crowder. 2004. The binding of iron and zinc to glyoxalase II occurs exclusively as di-metal centers and is unique within the metallo-β-lactamase family. *J. Biol. Inorg. Chem.* 9:429–438.

59. Mangani, S., P. Carloni, …, J. E. Coleman. 1992. EXAFS study of the active site of alkaline phosphatase from *E. coli*. *Inorg. Chim. Acta.* 191:161–165.

60. Mitić, N., S. J. Smith, …, G. Schenk. 2006. The catalytic mechanisms of binuclear metallohydrolases. *Chem. Rev.* 106:3338–3363.

61. Tran, H. T., B. A. Hurley, and W. C. Plaxtona. 2010. Feeding hungry plants: the role of purple acid phosphatases in phosphate nutrition. *Plant Sci.* 179:14–27.

62. Kauzlarich, S. M., B. K. Teo, …, B. A. Averill. 1986. X-ray absorption studies on the purple acid phosphatase from beef spleen. *Inorg. Chem.* 25:2781–2785.

63. Klabunde, T., N. Sträter, …, B. Krebs. 1996. Mechanism of Fe(III)-Zn(II) purple acid phosphatase based on crystal structures. *J. Mol. Biol.* 259:737–748.

64. Guddat, L. W., A. S. McAlpine, …, J. L. Martin. 1999. Crystal structure of mammalian purple acid phosphatase. *Structure.* 7:757–767.

65. True, A. E., R. C. Scarrow, …, L. Que, Jr. 1993. EXAFS studies of uteroferrin and its anion complexes. *J. Am. Chem. Soc.* 115:4246–4255.

66. Wang, X., C. R. Randall, …, L. Que, Jr. 1996. X-ray absorption spectroscopic studies of the FeZn derivative of uteroferrin. *Biochemistry.* 35:13946–13954.

67. Wang, X., and L. Que, Jr. 1998. Extended X-ray absorption fine structure studies of the anion complexes of FeZn uteroferrin. *Biochemistry.* 37:7813–7821.

68. Wang, X., R. Y. N. Ho, …, L. Que, Jr. 1999. Spectroscopic characterization of a ternary phosphatase-substrate-fluoride complex. Mechanistic implications for dinuclear hydrolases. *J. Am. Chem. Soc.* 121:9235–9236.

69. Schenk, G., R. A. Peralta, …, A. Neves. 2008. Probing the role of the divalent metal ion in uteroferrin using metal ion replacement and a comparison to isostructural biomimetics. *J. Biol. Inorg. Chem.* 13:139–155.

70. Walsh, C., and G. Wright. 2005. Introduction: antibiotic resistance. *Chem. Rev.* 105:391–394.

71. Crowder, M. W., J. Spencer, and A. J. Vila. 2006. Metallo-β-lactamases: novel weaponry for antibiotic resistance in bacteria. *Acc. Chem. Res.* 39:721–728.

72. Heinz, U., and H. W. Adolph. 2004. Metallo-β-lactamases: two binding sites for one catalytic metal ion? *Cell. Mol. Life Sci.* 61:2827–2839.

73. Bebrone, C. 2007. Metallo-β-lactamases (classification, activity, genetic organization, structure, zinc coordination) and their superfamily. *Biochem. Pharmacol.* 74:1686–1701.

74. Feiters, M. C., C. Little, and S. G. Waley. 1986. Metal coordination in zinc enzymes. *J. Phys. Colloq.* 47:1169–1172.

75. Paul-Soto, R., R. Bauer, …, H. W. Adolph. 1999. Mono- and binuclear Zn^{2+}-β-lactamase. Role of the conserved cysteine in the catalytic mechanism. *J. Biol. Chem.* 274:13242–13249.

76. de Seny, D., U. Heinz, …, H. W. Adolph. 2001. Metal ion binding and coordination geometry for wild type and mutants of metallo-β-lactamase from Bacillus cereus 569/H/9 (BcII): a combined thermodynamic, kinetic, and spectroscopic approach. *J. Biol. Chem.* 276:45065–45078.

77. González, J. M., F. J. Medrano Martín, …, A. J. Vila. 2007. The Zn2 position in metallo-β-lactamases is critical for activity: a study on chimeric metal sites on a conserved protein scaffold. *J. Mol. Biol.* 373:1141–1156.

78. Abriata, L. A., L. J. González, …, A. J. Vila. 2008. Engineered mononuclear variants in *Bacillus cereus* metallo-β-lactamase BcII are inactive. *Biochemistry.* 47:8590–8599.

79. Campos-Bermudez, V. A., J. M. González, …, A. J. Vila. 2010. Spectroscopic signature of a ubiquitous metal binding site in the metallo-β-lactamase superfamily. *J. Biol. Inorg. Chem.* 15:1209–1218.

80. Llarrull, L. I., M. F. Tioni, and A. J. Vila. 2008. Metal content and localization during turnover in *B. cereus* metallo-β-lactamase. *J. Am. Chem. Soc.* 130:15842–15851.

81. Llarrull, L. I., M. F. Tioni, …, A. J. Vila. 2007. Evidence for a dinuclear active site in the metallo-β-lactamase BcII with substoichiometric Co(II). A new model for metal uptake. *J. Biol. Chem.* 282:30586–30595.

82. Breece, R. M., L. I. Llarrull, …, D. L. Tierney. 2012. X-ray absorption spectroscopy of metal site speciation in the metallo-β-lactamase BcII from *Bacillus cereus*. *J. Inorg. Biochem.* 111:182–186.

83. Griffin, D. H., T. K. Richmond, …, M. W. Crowder. 2011. Structural and kinetic studies on metallo-β-lactamase IMP-1. *Biochemistry.* 50:9125–9134.

84. Yang, H., M. Aitha, …, D. L. Tierney. 2014. Spectroscopic and mechanistic studies of heterodimetallic forms of metallo-β-lactamase NDM-1. *J. Am. Chem. Soc.* 136:7273–7285.

85. Periyannan, G. R., A. L. Costello, …, M. W. Crowder. 2006. Sequential binding of cobalt(II) to metallo-β-lactamase CcrA. *Biochemistry.* 45:1313–1320.

86. Hawk, M. J., R. M. Breece, …, M. W. Crowder. 2009. Differential binding of Co(II) and Zn(II) to metallo-β-lactamase Bla2 from *Bacillus anthracis*. *J. Am. Chem. Soc.* 131:10753–10762.

87. Costello, A., G. Periyannan, …, D. L. Tierney. 2006. Site-selective binding of Zn(II) to metallo-β-lactamase L1 from *Stenotrophomonas maltophilia*. *J. Biol. Inorg. Chem.* 11:351–358.

88. Costello, A. L., N. P. Sharma, …, D. L. Tierney. 2006. X-ray absorption spectroscopy of the zinc-binding sites in the class B2 metallo-β-lactamase ImiS from *Aeromonas veronii bv. sobria*. *Biochemistry.* 45:13650–13658.

89. Sharma, N., Z. Hu, …, B. Bennett. 2008. Conformational changes in the metallo-β-lactamase ImiS during the catalytic reaction: an EPR spectrokinetic study of Co(II)-spin label interactions. *J. Am. Chem. Soc.* 130:8215–8222.

90. Breece, R. M., Z. Hu, …, D. L. Tierney. 2009. Motion of the zinc ions in catalysis by a dizinc metallo-β-lactamase. *J. Am. Chem. Soc.* 131:11642–11643.

91. Yang, H., M. Aitha, …, M. W. Crowder. 2012. Mechanistic and spectroscopic studies of metallo-β-lactamase NDM-1. *Biochemistry.* 51:3839–3847.

92. Mustre de Leon, J., J. J. Rehr, S. I. Zabinsky, and R. C. Albers. 1991. *Ab initio* curved-wave x-ray-absorption fine structure. *Phys. Rev. B Condens. Matter.* 44:4146–4156.

93. Ashley, C. A., and S. Doniach. 1975. Theory of extended x-ray absorption edge fine structure (EXAFS) in crystalline solids. *Phys. Rev. B.* 11:1279–1288.

94. Reference deleted in proof.

95. O'Day, P. A., J. J. Rehr, …, G. E. Brown, Jr. 1994. Extended x-ray absorption fine structure (EXAFS) analysis of disorder and multiple-scattering in complex crystalline solids. *J. Am. Chem. Soc.* 116:2938–2949.

96. Ankudinov, A. L., B. Ravel, …, S. D. Conradson. 1998. Real space multiple scattering calculation and interpretation of XANES. *Phys. Rev. B.* 58:7565–7576.

97. Reference deleted in proof.

98. Ankudinov, A. L., and J. J. Rehr. 2003. Development of XAFS theory. *J. Synchrotron Radiat.* 10:366–368.

99. Ankudinov, A. L., and J. J. Rehr. 2000. Theory of solid state contributions to the x-ray elastic scattering amplitude. *Phys. Rev. B.* 62:2437–2445.

100. Poiarkova, A. V., and J. J. Rehr. 1999. Multiple-scattering x-ray-absorption fine-structure Debye-Waller factor calculations. *Phys. Rev. B.* 59:948–957.

101. Rehr, J. J., R. C. Albers, and S. I. Zabinsky. 1992. High-order multiple-scattering calculations of x-ray-absorption fine structure. *Phys. Rev. Lett.* 69:3397–3400.

102. Rehr, J. J., J. Mustre de Leon, …, R. C. Albers. 1991. Theoretical x-ray absorption fine structure standards. *J. Am. Chem. Soc.* 113: 5135–5140.

103. Teo, B. K., and P. A. Lee. 1979. Ab initio calculations of amplitude and phase...x-ray absorption fine structure spectroscopy. *J. Am. Chem. Soc.* 101:2815–2832.

104. Gurnman, S. J., N. Binsted, and I. Ross. 1984. A rapid, exact, curved-wave theory for EXAFS calculations. *J. Phys. C.* 17:143–151.

Supporting Material

X-ray Absorption Spectroscopy of Dinuclear Metallohydrolases

David L. Tierney[†*] and Gerhard Schenk[‡]

[†]Department of Chemistry and Biochemistry, Miami University, Oxford, OH 45056, U.S.A.

[‡]School of Chemistry and Molecular Biosciences, The University of Queensland, St. Lucia, QLD 4072, Australia.

[*]Correspondence: tiernedl@miamioh.edu

Data Reduction

In practice, the EXAFS can be separated into two independent components: a smoothly varying background and an oscillatory interference pattern whose magnitude decreases monotonically with increasing energy. The smooth background represents the absorption of the free atom, which is usually unavailable, and is, therefore, approximated by fitting a 2-3 region spline (of quadratic or cubic polynomials) to the data above the edge (**Fig. S1**). The oscillatory portion of the spectrum that remains is a direct result of the local structure experienced by the absorbing atom. The damping of the oscillations as the energy increases is a measure of the disorder in the local structure, both static (variations in distance) and dynamic (thermal motion). While the static disorder cannot be experimentally controlled, the dynamic disorder, which is dominant near room temperature, can be effectively eliminated at cryogenic temperatures. The use of low temperature has the added benefit of reducing the radiation damage to the sample from prolonged exposure to high intensity ionizing radiation.

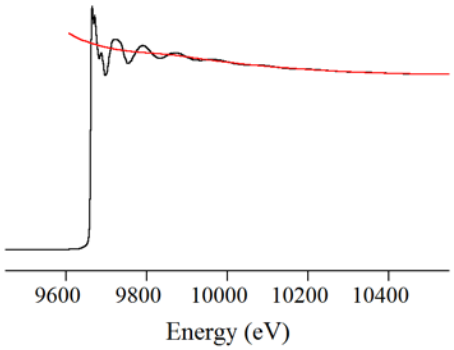

Fig. S1. Example of a spline background.

$$k = \frac{m_e v}{\hbar} = \frac{2\pi}{\lambda} = \left[\frac{2m_e}{\hbar^2}\left(E - E_0\right)\right]^{1/2} = \left[0.2625\left(E - E_0\right)\right]^{1/2} \qquad \text{(S1)}$$

Once isolated from the background, the EXAFS is typically subjected to Fourier analysis for frequency deconvolution. It is, therefore, useful to present the EXAFS as a function of the photoelectron momentum, or wave vector, *k*, (**Eq. S1**) which has units of inverse angstroms, $Å^{-1}$. This is analogous to photon momentum (wavenumber, cm^{-1}), except that, unlike a photon, the photoelectron has non-zero mass. Consequently, while

photon momentum is linearly dependent on its energy, photoelectron momentum is dependent on the square-root of its energy. **Eq. S1** holds for E expressed in electron volts (eV), where 1 eV = 1.6 x 10^{-19} J = 8066 cm^{-1}. In **Eq. S1**, m_e is the electron rest mass, h is Planck's constant and E_0 represents the energy required to promote an electron to the continuum (see **Fig. S1**). While E_0, which depends on the local structure of the metal ion, could, in principle, be experimentally obtained from X-ray photoemission spectroscopy (XPS), it is impractical to measure. Therefore, E_0 is either treated as a variable parameter in EXAFS analysis or held fixed at a calibrated value, obtained from analysis of a compound of known structure.

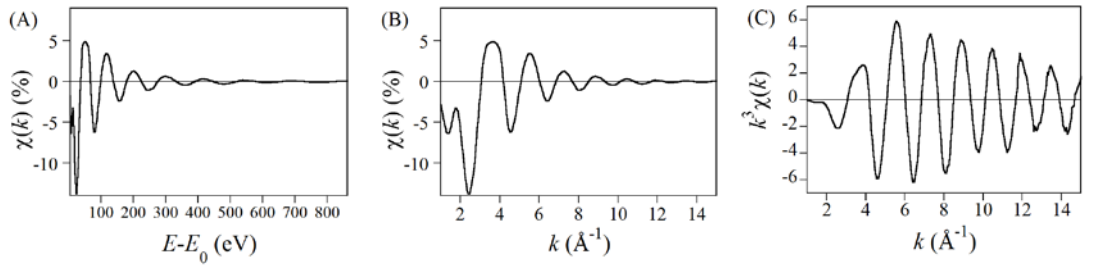

Fig. S2. Presentation of the background subtracted EXAFS for a ZnS_4 metal site (χ) (A) *vs.* energy above E_0, as a percentage of the atomic absorption (edge jump) (B) *vs. k* and (C) *vs. k*, weighted by k^3.

Care must be taken to keep the initial value of E_0 constant when comparing EXAFS datasets (typically 15-20 eV above E_0 for the elemental form of the metal of interest), as it is this initial value that sets the reference energy when the data are converted to *k*-space. Given the approximately k^3 decay of the EXAFS amplitude, it is common to display the raw EXAFS data weighted by k^3 to accentuate the oscillations at higher photoelectron momentum (**Fig. S2**). As is apparent in **Fig. S2**, the inherent signal-to-noise drops precipitously with increasing energy. Consequently, data integration times are also often scaled by k^3, so that the majority of the time invested in data collection is spent in the region where the signal intensity is lowest.

A Fourier transform (FT) takes the dependent variable into the inverse space of the independent variable. Therefore, an FT of the *k*-space EXAFS ($Å^{-1}$) has units of

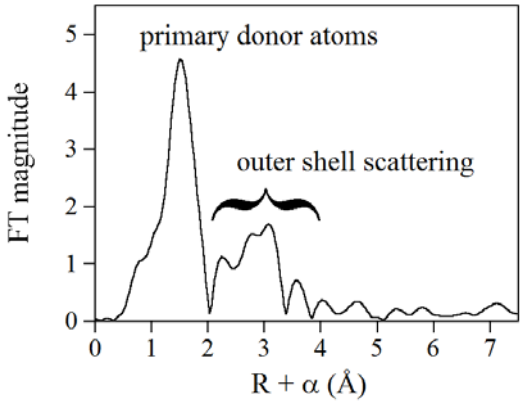

Fig. S3. EXAFS Fourier transform indicating the metal ion's primary coordination sphere and the outer shell scattering associated with rigidly held, distant atoms.

distance (Å). For randomly oriented samples, such as frozen solutions, the observed EXAFS is the sum of all possible orientations, and the FT represents a pseudo-radial distribution function (RDF) about the central atom. The peaks in the FT then represent a group of atoms at a similar distance (referred to as "shells," **Fig. S3**). It is not a true RDF because of the phase-shift (ϕ_{as}) experienced by the photoelectron as it passes through the atomic potentials (electron clouds) of the absorber and the scatterer (typically *ca.* -0.4 Å in *R*-space). In recent years, it has become common to present phase-shifted Fourier transforms, where the phase-shift is applied *prior* to Fourier transformation, effectively displaying the data on a "true" distance axis (*R*, rather than $R + \alpha$). However, this point deserves a word of caution. As different atoms with different atomic potentials will necessarily produce a different phase-shift, the phase-shift is unique to a given absorber-scatterer pair. Only one phase-shift can be applied to the data prior to Fourier transformation, making this is a dangerous practice for a heterogeneous metal site with mixed N/O/S donor sets, potentially obscuring minor contributors, such as the single sulfur donor in the dinuclear active site of class B1 metallo-β-lactamases (0.5 S per Zn, see text).

While the FT is useful for visualization of the data, it is the *k*-space data that are fit in determining the most consistent structural model. The use of Fourier filtering (forward transformation, Gaussian windowing and back-transformation into *k*-space) allows deconvolution of the observed EXAFS into its component frequencies (**Fig. S4A**) and can be used to remove high frequency noise (**Fig. S4B**). However, as with any Fourier transform, the reverse FT is sensitive to the endpoints chosen. In particular, when

frequencies differ by distances close to the resolution of the data (below), the two peaks overlap significantly in the FT and they may effectively cancel, leading to a false zero point. If this false zero is used as one of the window limits, real contributions can be unintentionally removed by the Fourier filter, leading to exclusion of a shell of scatterers that is actually present. An example of this is shown below. It is, therefore, critical that any analysis be carried out on both filtered and unfiltered data to ensure the consistency of the model.

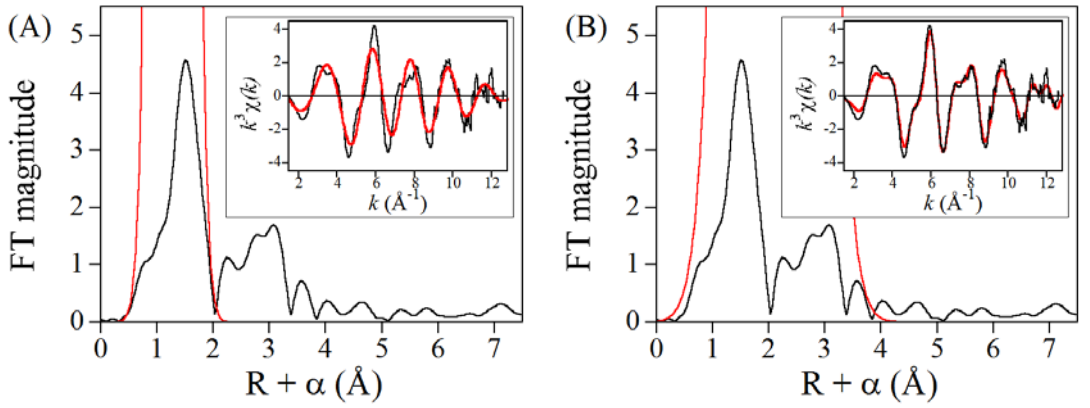

Fig. S4. Application of a Gaussian window and Fourier filtering (A) to isolate a particular shell or (B) to remove high frequency noise.

EXAFS Data Fitting

Most EXAFS analysis software starts from the plane-wave approximation, which assumes the inter-atomic distance is large relative to the photoelectron momentum, allowing its description as a planar wave propagating with uniform velocity along the vector that connects the absorbing and scattering atoms. Above $k \sim 1$ Å^{-1}, this assumption is valid. The curved-wave approximation takes the angular variation of propagation into account, allowing extension of the data analysis below $k = 1$ (92). The most simplistic interpretation of EXAFS is the single-scattering (SS) formalism (93, 94). This approach assumes that the only phenomena observed are two-body, single-scattering events. The advantage of the SS formalism is its simplicity. However, this approach neglects

scattering pathways involving three or more atoms and thus ignores any angular information that may be contained in the EXAFS. Recent theoretical advances have made multiple scattering calculations more straightforward, allowing inclusion of scattering events involving 3 or more atoms in the analysis (95-102).

$$\chi(k) = \sum \frac{N_{as} A_s(k) S_c}{kR_{as}^{\ 2}} \exp(-2k^2 \sigma_{as}^{\ 2}) \exp(-2R_{as}/\lambda) \sin[2kR_{as} + \phi_{as}(k)] \qquad \text{(S2)}$$

$$R = \frac{\sum_{i=1}^{N} \left(\chi_{i,obs} - \chi_{i,calc}\right)^2}{\sum_{i=1}^{N} \left(\chi_{i,obs}\right)^2} \qquad \text{(S3)}$$

The EXAFS can be described, to first order, by **Eq. S2**. Structural information is extracted from the EXAFS *via* a least-squares fit to **Eq. S2**. The quality of the fit is judged by the magnitude of some form of fit residual, such as that given in **Eq. S3**, where a smaller residual indicates smaller deviation between the model and the data (*i. e.*, a better model). In **Eq. S2**, N_{as} represents the number of like atoms at a given distance from the absorber (the number of atoms in a shell); S_c is the scale factor, which is specific to the absorber-scatterer (*as*) pair and largely independent of energy; $A_s(k)$ represents the backscattering power of the scattering atom; R_{as} is the average absorber-scatterer interatomic distance. The sum is taken over all shells of scatterers. The first exponential damping term, exp ($-2k^2\sigma_{as}^{\ 2}$), where σ_{as} is the rms variation in R_{as} (assuming thermal disorder is negligible), is known as the Debye-Waller factor. The second damping term, exp ($-2R_{as}/\lambda$), where λ is the mean free path of the photoelectron, accounts for losses in amplitude due to inelastic scattering of the photoelectron. These first three terms in **Eq. S2** derive from evaluation of the first moment of the EXAFS and define the observed amplitude. The amplitude effectively represents the probability of photoelectron scattering, which depends on both the identity of the scattering atom (larger atoms = larger probability) and the number of scattering atoms. The combination of similarity in

size and similar phase shifts affected by atoms within the same period makes it difficult to distinguish scattering atoms within Z ~ 8 (such as N and O), but relatively easy to distinguish scatterers from different rows of the periodic table (such as N/O and S). This point is illustrated in **Fig. S5** for zinc-nitrogen and zinc-sulfur scattering, which are out of phase over most of the *k*-range that is common to EXAFS studies of metalloproteins.

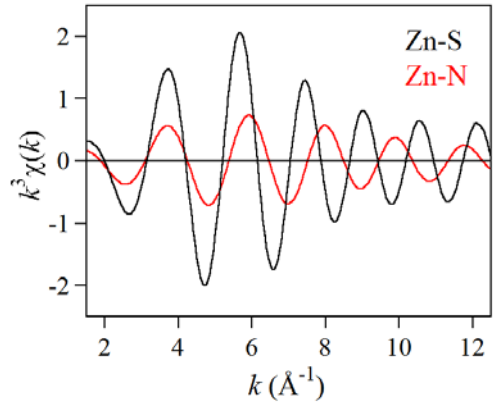

Fig. S5. Relative phases of Zn-N (2.00 Å) and Zn-S (2.30 Å) scattering.

The final term in **Eq. S2**, $\sin[2kR_{as} + \phi_{as}(k)]$, comes from evaluation of the second moment of the EXAFS, and defines the frequency of the oscillations. Its linear dependence on the absorber-scatterer distance illustrates how the frequency of the EXAFS provides direct information on distance. Short distances produce low-frequency oscillations, while longer distances lead to higher frequency oscillations. Also included in the argument of the sine function is $\phi_{as}(k)$, the aforementioned phase-shift experienced by the photoelectron as it passes through the atomic potentials of the absorbing and scattering atoms. In order to extract structural information from the EXAFS, it is necessary to provide the amplitude ($A_s(k)\exp(-2R_{as}/\lambda)$) and phase ($\phi_{as}(k)$) functions for each absorber-scatterer pair. These functions may be obtained either empirically, from the measured EXAFS of a structurally characterized small molecule, or, as is more common, by one of several theoretical calculations (96, 103, 104).

Use of theoretical amplitude and phase functions to fit data from an unknown structure requires that the scale factor (S_c) and the shift in E_0 (ΔE_0) be calibrated by fitting EXAFS data for crystallographically characterized small molecules, in order to minimize the number of variable parameters in fitting the unknown data (discussed

further below). In general, fits to model data will refine S_c, ΔE_0, σ_{as} and $R_{as,}$ while holding the coordination number fixed at the crystallographically determined value. Provided this fit gives the correct bond length with a reasonable value of σ_{as}, the refined values of S_c and ΔE_0 can then be used, and held fixed, in fits to the EXAFS data for unknown systems. It is important to realize that S_c is an absorber-scatterer dependent parameter. Each type of scattering interaction will have a different optimal value. In contrast, E_0 (and, therefore, ΔE_0) is defined by the metal ion. Consequently, while there is still some debate on this issue, it is largely accepted that a single value of ΔE_0 should be used for all shells included in a fit. Caution should be used when refining ΔE_0, as this is equivalent to refining the phase-shift in the course of the fit.

Limitations

There are, essentially, three observables in an EXAFS spectrum: amplitude, frequency and phase. From the amplitude of the observed EXAFS, the scatterer identity, coordination number and relative disorder can be determined. However, these parameters are highly correlated. For example, if the data are fit with a coordination number that is higher than the true coordination number, σ_{as} will refine to an unreasonably large value to reduce the apparent amplitude. In practice, the EXAFS coordination number is determined with an accuracy of *ca.* 25%, or ± 1, although the precision is significantly better.

In contrast to the amplitude, the frequency of the EXAFS, and thus the distance obtained, is very well determined. The absorber-scatterer distance is usually accurate to ± 0.02 Å, with a precision of ± 0.005 Å. As such, the average bond length derived from a least-squares fit to the first shell is a strong indicator of the metal ion's primary coordination number. Comparison of average metal-ligand bond lengths from small molecule crystal structures shows that, in general, an increase of ~ 0.1 Å can be anticipated for each additional ligand. For example, a survey of the Cambridge

Crystallographic Database shows average bond lengths of 1.95, 2.07 and 2.18 Å for 4-, 5- and 6-coordinate Zn(II), respectively, with all nitrogen donors. These values will shorten slightly for every nitrogen donor that is replaced with an oxygen donor, and lengthen for every nitrogen donor that is replaced with a sulfur donor.

$$\Delta R = \frac{\pi}{2\Delta k} \qquad N_{idp} = \frac{2\Delta R \Delta k}{\pi} \tag{S4}$$

As with any least-squares procedure, a good fit can always be obtained with a sufficient number of variable parameters. The corollary to that statement is that a *better* fit will always be obtained with *more* variable parameters. It is, therefore, important to understand the limitations of the information content of an EXAFS spectrum. The inherent distance resolution of a set of EXAFS data is inversely proportional to the span of the data in *k*-space ($\Delta k = k_{max}$-k_{min}, **Eq. S4**). Inspection of **Eq. S4** shows that in order to distinguish two shells separated by 0.10 Å, the *k*-range of the data must be at least 15.7 Å^{-1}. Typically, EXAFS spectra for a biological sample will span Δk ~ 10-12 Å^{-1}, carrying 0.16 – 0.13 Å resolution. Thus, a multi-component fit that refines to distances that differ by less than this value cannot be considered a valid model.

Eq. S4 also defines the number of independent points, N_{idp}, in an EXAFS dataset, which is an indication of the number of variable parameters that can be refined with confidence. For a single shell of scatterers, ΔR will be on the order of 1.2 Å, giving a total of *ca.* 8 independent points for Δk = 10 Å^{-1}. This value is larger than the five parameters that can be varied for a single shell (ΔE_0, S_c, N_{as}, R_{as} and σ_{as}), and in refining all five, the variables will be slightly over-determined. However, addition of a second type of scatterers would double the number of variables, and the fit would then be under-determined. Thus, it is important to carefully control, or at least be cognizant of, the number of variable parameters used to fit the data. The most common approach to controlling the number of refined variables is to hold ΔE_0 and S_c fixed at calibrated

values, obtained as described above, refining R_{as} and σ_{as}, and stepping N_{as} through all reasonable integer or half-integer values, using the fit residual to define the best-fit coordination number.

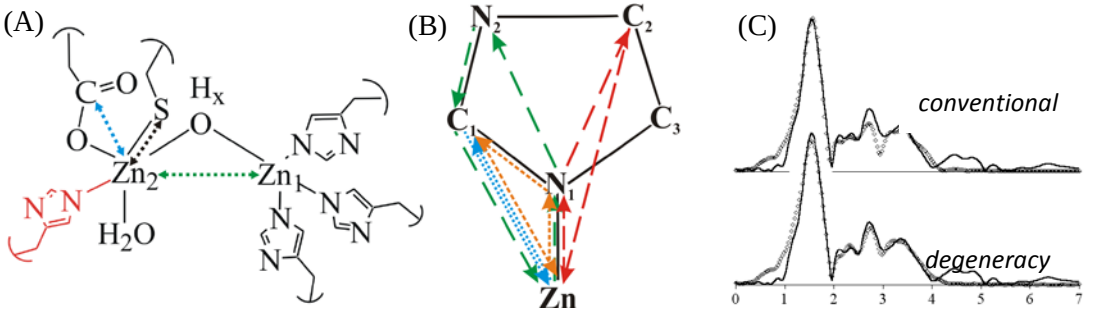

Fig. S6. (A) Active site of a B1 M
to its EXAFS data. (B) Subset of the multiple scattering pathways available with a coordinated imidazole. (C) Comparison of fits to $[Zn(Im)_4]^{2+}$ EXAFS data using conventional method and degeneracy-based method.

Deconvolution of a complex metal site

It is useful to define a strategy for fitting the data from a complex metal site. As much of the mini-review deals with EXAFS data of metallo-β-lactamases (MβLs), we will outline the strategy in use in our laboratories, in the context of a class B1 MβL, which has two Zn(II) ions in its active site. One of the Zn(II) ions is coordinated by three histidine side chains and a water molecule that bridges the two metals. The second Zn(II) is coordinated by one of every biologically relevant ligand: a monodentate carboxylate (asp), one histidine, one cysteine, a terminal water molecule and the bridging solvent (**Fig. S6**). The *average* Zn(II) coordination sphere consists of 4 N/O and 0.5 S donors in the primary coordination sphere, with two histidine side chains, a Zn-Zn interaction and possibly a carboxylate carbon contributing to the outer shell scattering (**Fig. S3**). As EXAFS is a bulk measurement, it is this average environment that will be detected. The approach outlined below is certainly not the only one that has been employed, nor is it the

only one that is valid. We developed this protocol purely with an eye on being conservative in our interpretation of the data.

The most difficult aspects of EXAFS analysis of a metal site such as this are reliable identification of the Zn-S scattering and extraction of the Zn-Zn interatomic distance in the presence of a relatively large background of imidazole outer shell scattering. Identification of the sulfur donor is complicated by its low occupation (1 out of 9 ligands) and the presence of the carboxylate carbon atom which resides at a similar distance (~ 2.5 Å relative to ~ 2.3 Å for the Zn-S). These interactions can effectively cancel each other when the carboxylate is held in a well-ordered configuration, as these two interactions will be out of phase with each other. The net result is that the apparent contribution of the Zn-S scattering path is reduced as the two distances converge, as illustrated in **Fig. S7**.

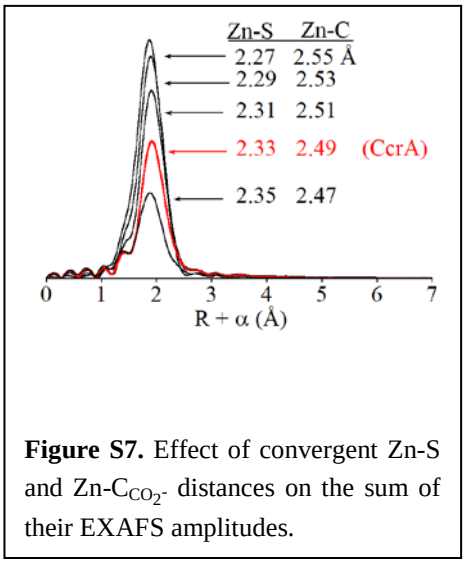

Figure S7. Effect of convergent Zn-S and Zn-C_{CO_2}- distances on the sum of their EXAFS amplitudes.

Multiple scattering interactions from within the rigid ring system of a coordinated imidazole are well known in metalloprotein EXAFS, producing four features of near equal intensity in the FT (see **Fig. S6**), and a number of approaches to their quantification have been put forth. In principle, the observed scattering pattern contains both distance and angular information, although the angular information is difficult to extract, especially when more than one such ligand is present. A full multiple-scattering calculation of a simple metal-imidazole interaction, such as that shown in **Fig. S6**, will identify 140 distinct scattering paths, 35 of which are predicted to display intensities of 10% or greater relative to the metal-nitrogen single-scattering pathway. The most historically common approach to fitting imidazole outer shell scattering fits the four most prominent scattering pathways to the data, allowing R_{as} and σ_{as} for each to refine,

holding their coordination numbers fixed at the degeneracy of the path, as defined by the calculation. The disadvantage of this approach is that it neglects 21 of the 35 paths that produce significant scattering intensity. Newer software packages allow the linking of multiple pathways, affording the opportunity to fix the imidazole ring as a rigid unit, refining all of the distances in a correlated fashion. This, however, enforces idealized bond angles on the metal-histidine interaction that may not be representative of the real arrangement.

We have taken a more pragmatic approach to this problem. If one accepts that there is angular variability, and that this cannot be easily predicted, then it is better to refine all of the metal-histidine associated paths independent of one another. Given that the degeneracy of the most prominent paths only account for 14 of the 35 paths with significant scattering power, we chose to include them indirectly by grouping them by distance relative to the four most prominent. We then replace the degeneracy of the individual paths with the sum degeneracy of paths of similar length. In our hands, this approach produces a better fit to all four outer shell features (see **Fig. S6C**), which is critical to extraction of the metal-metal scattering in these systems, with one single atom bridge and separations of *ca.* 3.4 Å.

The process we follow is straightforward, as outlined in **Fig. S8**. Starting with the Fourier-filtered first shell (**Fig. S4A**), we first fit it with low-Z (N/O) scatterers and determine their best fit coordination number, in half-integer steps, determined by that which produces the smallest fit residual (**Eq. S3**). We then add S scatterers, also in half-integer steps, monitoring the improvement in the fit residual, with fits that produces less than ~ 50 % improvement considered unjustified. Once the best first shell fit has been obtained, we return to the full spectrum (**Fig. S4B**), fitting the Fourier-filtered data for the sake of comparing smaller fit residuals. Using the full span of the data, we add in imidazoles, again in half-integer steps, reporting that which produces the smallest fit residual. We estimate the uncertainty in the number of imidazole scatterers determined in

this way to be ± 0.5. It is at this point that we add in the metal-metal scattering pathway, again looking for a significant reduction in fit residual. Using this procedure, improvements of 40 – 70 % are attainable for well-ordered systems. Generally, fits that produce smaller improvements are not interpreted as indicative of metal-metal scattering, and the metal-metal path is not reported. For each step in fitting the full dataset (with and without inclusion of metal-metal scattering), we compare the basic N/O/S + imidazole (± metal-metal) fit to one that includes a metal-carbon shell, to assess the potential effect of the carboxylate carbon on the overall model. Again, we stress here that all Fourier-filtered fits are compared to fits to the as-isolated *k*-space data, to ensure the reliability of the fit.

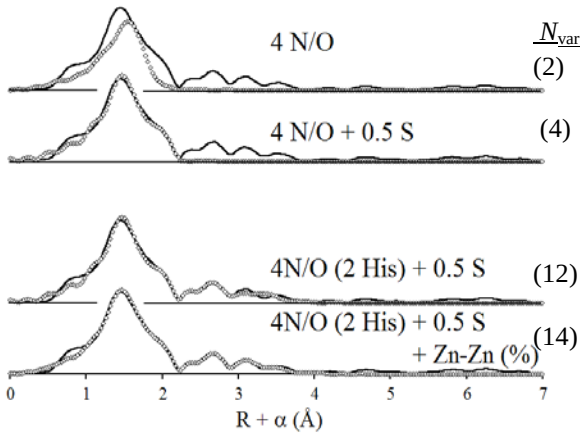

Fig. S8. Stepwise process of building up a structural model consistent with the EXAFS of an MβL.

Experimental considerations.

The general setup of an XAS experiment is shown in **Fig. S9**. The experiment involves stepping through the incident X-ray energy while measuring incident (I_0) and transmitted (or fluorescent) X-ray intensity (I_1 or FF). X-ray intensity is measured using gas-filled ionization chambers (I_0, I_1 and I_2) that consist of a large surface area capacitor whose plates are parallel to the direction of light propagation. The X-ray beam passing between the plates ionizes the gas

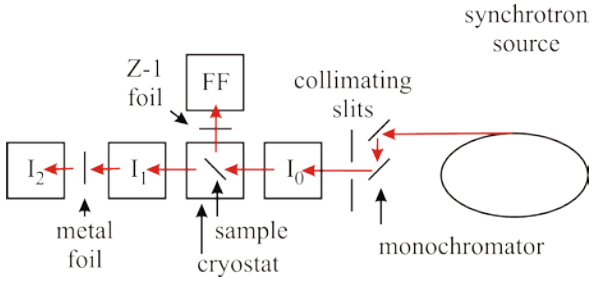

Figure S9. Schematic of an XAS experimental setup.

in the chamber, allowing current flow between them, proportional to the photon density per unit time. Monochromatic radiation is typically obtained by using an in-line double crystal monochromator, taking advantage of Bragg reflection ($n\lambda = 2d\sin\theta$) from specific crystal planes. The double crystal design allows the monochromatic radiation to exit the monochromator parallel to the incident radiation, maintaining constant beam position relative to the experimental setup, independent of the energy selected. To ensure accurate calibration of the energy, the XAS spectrum of a metal foil (positioned between I_1 and I_2 in **Fig. S9**) is measured at the same time as the experimental spectrum. The first inflection point of the spectrum from the elemental form of a metal occurs at a well-defined energy, and it is this point that is used to calibrate the experimental spectrum.

$$\Delta E = E(\Delta\theta)\cot\theta \qquad \text{(S5)}$$

The energy resolution is dependent on a number of factors. For a conventional flat crystal monochromator, the energy resolution is given by **Eq. S5**. In **Eq. S5**, θ is the Bragg angle at energy E, while $\Delta\theta$ is the spread in θ, which is defined by the vertical collimation of the X-ray source and the vertical divergence of the synchrotron source. Thus, the energy resolution is affected by the vertical size of the incident beam (*i. e.*, larger vertical size = lower energy resolution), which is defined by the collimating slits in **Fig. S9**. The breadth of the rocking curve (range of θ), and therefore the energy resolution, of a given crystal set is inversely proportional to the *d*-spacing of that crystal. Thus, better energy resolution is obtained with Si(220) crystals, with a *d*-spacing of 1.92 Å, than with Si(111) crystals, with a *d*-spacing of 3.14 Å.

By definition, Bragg reflection contains contributions from higher order harmonics ($n > 1$), in addition to the fundamental frequency. For example, a Si(220) monochromator set to deliver 9 keV photons will also pass 18 keV photons. Therefore, the experimental setup must include some method of harmonic rejection. The two most common methods of harmonic discrimination are “de-tuning” the monochromator and

use of an in-line mirror (between the monochromator and the collimating slits in **Fig. S9**). The former takes advantage of the narrower rocking curve for reflection of the harmonic compared to the fundamental, reducing the harmonic content of the reflected radiation by rotating one of the crystals in a double crystal setup slightly off parallel. The disadvantage of this simple approach is that it simultaneously reduces the incident intensity of *both* the fundamental and the harmonic, reducing the amount of the desired signal that is detected. The in-line mirror allows use of the full intensity of the incident X-ray beam. The angle of the mirror relative to the incident x-ray beam allows external reflection of the fundamental frequency, while higher harmonics are absorbed *via* total internal reflection.

XAS spectra of may be collected as transmission ($\ln(I_0/I_1)$ *vs. E*) or flourescence excitation spectra (FF/I_0 *vs. E*, using a fluorescence detector oriented normal to the incident X-ray beam), depending on the concentration of the analyte. For concentrations of *ca.* 20 mM or higher, the transmission experiment will afford better results. For metalloproteins, where concentrations are often limited to ~ 1 mM, K_α fluorescence excitation spectra offer greater sensitivity, particularly with the development of energy-discriminating solid-state detectors (the number of K_α photons emitted by the sample is directly proportional to the number of photons absorbed). However, fluorescence detection is typically limited in the number of photons that can be counted per unit time. As the fluorescence detector will see both fluorescent photons and elastically scattered photons (the strength of the solid state detector is the ability to distinguish them), the total incident count rate limits the photon density that can be employed. Contributions from the elastic scatter can be decreased by use of a low pass filter, typically the *Z*-1 metal foil placed in front of the fluorescence detector (*e. g.*, a Cu foil filter is used for measurement of Zn XAS).

Finally, it should be noted that any XAS experiment is only as good as the samples employed. Two key points should always be kept in mind. First, the reader is

reminded that XAS is a macroscopic technique that samples *all* populations of a given element in a sample. Therefore, it is critical that *all* of the metal of interest in a sample resides in a homogeneous environment. Any adventitiously bound metal will contribute to the measured EXAFS, giving a weighted average of all of the structures that are present. Second, the reader is reminded that diffraction occurs in all directions. The presence of ice crystals in a sample can effectively destroy an XAS experiment, as diffraction is much stronger than fluorescence, introducing artifacts into the spectrum that may, or may not, be obvious. For this reason, it is desirable to include a glassing agent, such as glycerol, to prevent formation of ice crystals on freezing.

REFERENCES

92. Mustre de Leon, J., J. J. Rehr, S. I. Zabinsky, and R. C. Albers. 1991. *Ab initio* Curved-Wave X-Ray-Absorption Fine Structure. *Phys. Rev. B* 44:4146-4156.
93. Ashley, C. A. and S. Doniach. 1975. Theory of extended x-ray absorption edge fine tructure (EXAFS) in crystalline solids. *Phys. Rev. B* 11:1279-1288.
94. Stern, E. A., D. E. Sayers, and F. W. Lytle. 1975. Extended x-ray-absorption fine-structure technique. III. Determination of physical parameters. *Phys. Rev. B* 11:4836-4846.
95. O'Day, P. A., J. J. Rehr, S. I. Zabinsky, and G. E. Brown, Jr. 1994. Extended X-Ray Absorption Fine Structure (EXAFS) Analysis of Disorder and Multiple-Scattering in Complex Crystalline Solids. *J. Am. Chem. Soc.* 116:2938-2949.
96. Ankudinov, A. L., B. Ravel, J. J. Rehr, and S. D. Conradson. 1998. Real Space Multiple Scattering Calculation and Interpretaton of XANES. *Phys. Rev. B* 58:7565-7576.
97. Rehr, J. J. and A. L. Ankudinov. 2005. Progress in the theory and interpretation of XANES. *Coord. Chem. Rev.* 249:131-140.
98. Ankudinov, A. L. and J. J. Rehr. 2003. Development of XAFS Theory. *J. Synchrotron Rad.* 10:366-368.
99. Ankudinov, A. L. and J. J. Rehr. 2000. Theory of Solid State Contributions to the X-Ray Elastic Scattering Amplitude. *Phys. Rev. B* 62:2437-2445.
100. Poiarkova, A. V. and J. J. Rehr. 1999. Multiple-Scattering X-ray-Absoption Fine-Structure Debye-Waller Factor Calculations. *Phys. Rev. B* 59:948-957.
101. Rehr, J. J., R. C. Albers, and S. I. Zabinsky. 1992. High-Order Multiple-Scattering Calculations of X-Ray-Absorption Fine Strucutre. *Phys. Rev. Lett.* 69:3397-3400.
102. Rehr, J. J., J. Mustre de Leon, S. I. Zabinsky, and R. C. Albers. 1991. Theoretical X-Ray Absorption Fine Structure Standards. *J. Am. Chem. Soc.* 113:5135-5140.
103. Teo, B. K. and P. A. Lee. 1979. *J. Am. Chem. Soc.* 101:2815-2832.
104. Gurnman, S. J., N. Binsted, and I. Ross. 1984. *J. Phys. C: Solid State Phys.* 17:143-151.